Comparing experimental sensitivities of Dark Matter experiments

Research Thesis

Presented in partial fulfillment of the requirements for graduation *with research distinction* in Physics in the undergraduate colleges of The Ohio State University

by

Boyu Gao

the Ohio State University

April, 2021

Abstract

The complementarity of dark matter experiments can be evinced from comparing their sensitivities to a given model. This thesis presents an introduction to dark matter, an overview of its detection methods, the model-dependent methods for comparing collider searches with dark matter indirect detection searches, and approaches comparing dark matter experiments in the weak dark mediator – quark coupling regime. The corresponding code for Monte Carlo simulation and an analysis framework for a mono-jet search at colliders is also available as part of this thesis: `https://github.com/Boyu622/MCsetup_monojet.git`

My contributions in this thesis are:

- Chapter 4.1: interpret dark matter annihilation cross section on its constraints at colliders, study the branching ratios for different DM annihilation channels, and solve a double mapping problem while translating the collider limits.
- Chapter 4.2: compute Gamma Ray spectra at production for all annihilation channels with varying m_{DM}, merge MadDM into the code for model dependent branching ratio calculation, script the whole procedure as an Indirect Detection tool, and constrain joint Dark Matter annihilation cross section with Fermi published data.
- Chapter 5: compare low g_q dark matter to understand the complementarity of dark matter experiments in this regime.
- Chapter 6: validate MadGraph NLO, Pythia8 + Rivet(Yoda) software chain, and study different showering scheme and matching parameters.

Acknowledgments

I want to thank:

- My advisors, Antonio Boveia and Caterina Doglioni, for their constant support and advice during the past two years on physics and my career.
- Linda Carpenter for help reproduce the dark matter indirect detection limit. José Zurita, Víctor Lozano, Rosa Seoane and John Stupak III for their assistant on validating the Monte Carlo simulation framework. Katherine Pachal for her support on analytically scaling the mono-jet signal cross section. Emma Tolley for teaching me the basics of dark matter. And K. K. Gan as the committee member of this thesis.
- My mother, aunt, and Xu Shuo for accompanying me on this journey.

Contents

Chapter 1

Introduction

There is convincing evidence that Dark Matter (DM) is necessary to make our cosmological observations consistent with our current understanding of gravity [1]. The Weakly Interacting Massive Particle (WIMP) hypothesis of DM is proposed by many theories [2], and is popular in the sense that it arises in many extensions of the Standard Model (SM) of Particle Physics [3]. WIMP Dark Matter couples weakly to the SM and can be probed, for example, by Collider [4] or Accelerator [5] searches, Direct Detection [6] and Indirect Detection [10]. In this thesis, the DM sensitivities of experimental searches at the Large Hadron Collider (LHC) are the main topic, and are summarized and compared with other non-collider results. The following overview in this chapter will be focusing on the evidence for Dark Matter from astrophysics and cosmology.

1.1 Galactic Rotation Curves

A direct evidence of DM comes from the rotation curves of galaxies. The visible mass $M_{visible}$ of a galaxy is concentrated inside the optical disc, and the expected

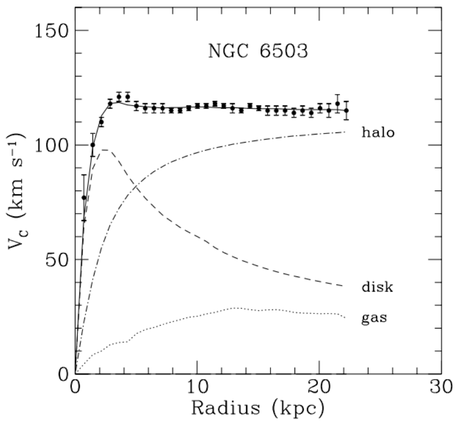

Figure 1.1: Adapted from [12]. Rotation curve of NGC 6503. v_c is plotted with respect to distance from galactic center.

orbiting velocity v_{exp} of stars at radius r from the prediction of Newtonian dynamics:

$$v_{exp}(r) = \sqrt{\frac{GM_{visible}}{r}} \tag{1.1}$$

where G is gravitational constant. Therefore, the expected circular velocity beyond the edge should be falling proportionally to the inverse of the square root of the galaxy's radius, $\propto 1/\sqrt{r}$. However, from observation in Figure 1.1, the circular velocities in this region exhibit flat behavior, where the expected velocities are plotted in dotted and dashed lines taking into account the gas and disk components respectively. The discrepancy between visible and indirectly measured mass can be solved by introducing an additional halo made of invisible matter as shown in dash-dotted line with $M(r) \propto r$ and $\rho(r) \propto 1/r^2$ [1].

1.1.1 Galactic Dark Matter profiles

A general DM halo with three parameters is given by [13], where α, β and γ are positive parameters:

$$\rho_{DM}(r) = \rho_0(\frac{r}{r_s})^{-\gamma}(1 + (\frac{r}{r_s})^{\alpha})^{(\gamma-\beta)/\alpha} \tag{1.2}$$

Here, the sharpness of inner slope and outer slope are controlled by γ and β, respectively. The parameter α controls the sharpness of the transition from inner slope to outer slop and r_s is the characteristic scale of galaxies. The Navarro-Frenk-White (NFW) profile is recovered when $(\alpha,\beta,\gamma) = (1,3,1)$ [14], which is a favored DM profile in galaxy formation mentioned in the same article. Additionally, as mentioned in this article [15], a weakly-cusped profile is modeled with $(\alpha,\beta,\gamma) = (1,3,1/2)$ and a cored profile is model with $(\alpha,\beta,\gamma) = (2,5,0)$.

1.2 Relic Abundance

In the early universe, $T > m_\chi$, where T is the temperature of the early universe, m_χ is the dark matter mass, and in natural units scheme T and mass have units of energy. Standard Model (SM) particles and antiparticles, f and $\bar{f}$, will then have enough kinematic energy to annihilate into DM particles and antiparticles, χ and $\bar{\chi}$. Thermal equilibrium of DM and SM particles is maintained this way via DM annihilation to SM particles $\chi\bar{\chi} \to f\bar{f}$, and DM production from SM particles $f\bar{f} \to \chi\bar{\chi}$. However, once $T < m_\chi$, the DM production rate is suppressed. The number density of DM will keep decreasing until the annihilation rate drops below the expansion rate of the universe. This is the freeze out point of DM, leaving a relic abundance of DM that can be measured today.

The relic abundance of DM can be obtained from measuring the Cosmic Microwave Background (CMB), which is the thermal background radiation created by photons decoupling from a photon-baryon fluid in the early universe [16]. From analyzing the small fluctuations of the CMB as results shown in Figure 1.2, the physical baryon density and physical matter density are found to be [18]:

$$\Omega_b h^2 = 0.022 \tag{1.3}$$

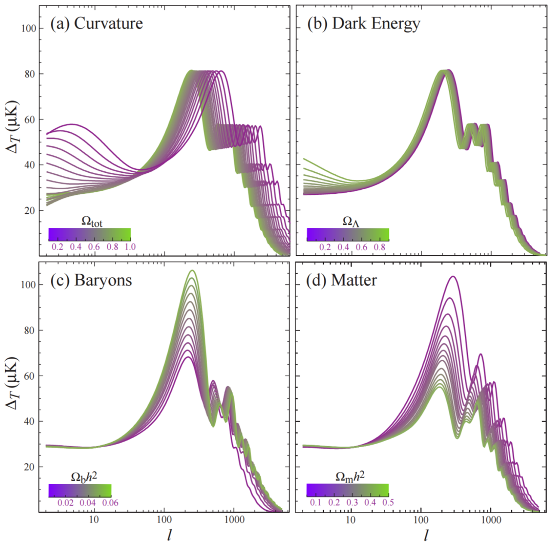

Figure 1.2: Adapted from [17]. Change of the CMB power spectrum with varying total curvature of the universe Ω_{tot}, dark energy density Ω_Λ, physical baryon density $\Omega_b h^2$ and physical matter density $\Omega_m h^2$.

$$\Omega_m h^2 = 0.14 \tag{1.4}$$

where h is the Hubble constant in units of 100 $kms^{-1}Mpc^{-1}$. Ω_b and Ω_m are baryon and matter density parameters defined as their density ratio with the critical density of the universe, which is the density the universe would have to have today in the absence of spatial curvature or a cosmological constant.

The dark matter density, with its density parameter Ω_c, is included in the matter density and can be extracted simply by subtracting the two. The result is:

$$\Omega_c h^2 = 0.12 \tag{1.5}$$

1.2.1 Constraining WIMP Dark Matter annihilation

The equation for DM particle number density before the freeze out is [1]:

$$\frac{dn}{dt} + 3Hn = -\langle \sigma v \rangle \left(n^2 - (n^{eq})^2\right) \tag{1.6}$$

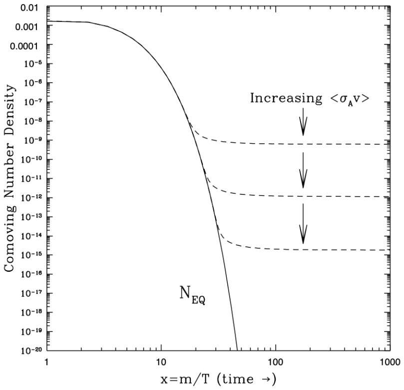

Figure 1.3: Adapted from[2]. Co-moving number density of WIMP DM in early Universe.

$\langle \sigma v \rangle$ is the thermal average of DM total annihilation cross section times velocity, n is the total DM number density, n^{eq} is the DM number density at thermal equilibrium and H is the Hubble constant. The right hand side of equation 1.6 quantifies how often the annihilation process takes place in unit time and volume. This is achieved by subtracting the thermal DM interaction where DM production also takes place. Together with the volume expansion effect of the universe, we find how the DM number density changes with respect to time.

For heavy WIMP states, the Maxwell-Boltzmann approximation for n^{eq} and non-relativistic expansion for $\langle \sigma v \rangle$ hold. Therefore, $n^{eq} \propto e^{-m/T}$ as in the Maxwell-Boltzmann distribution, which is shown as solid line in Figure 1.3. One can then obtain an order-of-magnitude result:

$$\Omega_c h^2 \approx \frac{3 \times 10^{-27} cm^3 s^{-1}}{\langle \sigma v \rangle} \tag{1.7}$$

The relationship between $\langle \sigma v \rangle$, the relic density and expansion of universe are shown as dashed line in the same figure. We can see that a higher DM annihilation cross section leads to a later freeze out and lower relic abundance. Comparing with the CMB measurement of relic density, we find that $\langle \sigma v \rangle_{WIMP} \sim 3 \times 10^{-26}\ cm^3 s^{-1}$.

Chapter 2

Models Considered

This chapter introduces the models used as benchmarks for sensitivities comparison. These models assume that DM particle is a Dirac fermion χ with an additional mediator particle mediating s-channel SM-DM interactions, called a $Z^{'}$. These are DM simplified models [19, 21], and have been adopted as LHC benchmarks since they are simple descriptions of collider phenomenology that capture common features across many WIMP models, while ignoring the differences among these models at energies higher than collider scales [4].

2.1 Vector and Axial-Vector models

Two spin-1 $Z^{'}$ mediator fields are described by the Lagrangian [19, 21]:

$$\mathcal{L}_{vector} = -g_{DM} Z^{'}_{\mu}\bar{\chi}\gamma^{\mu}\chi - g_q \sum_{q=u,d,s,c,b,t} Z^{'}_{\mu}\bar{q}\gamma^{\mu}q - g_l \sum_{l=e,\mu,\tau} Z^{'}_{\mu}\bar{l}\gamma^{\mu}l \tag{2.1}$$

$$\mathcal{L}_{axial-vector} = -g_{DM} Z^{'}_{\mu}\bar{\chi}\gamma^{\mu}\gamma_5\chi - g_q \sum_{q=u,d,s,c,b,t} Z^{'}_{\mu}\bar{q}\gamma^{\mu}\gamma_5 q - g_l \sum_{l=e,\mu,\tau} Z^{'}_{\mu}\bar{l}\gamma^{\mu}\gamma_5 l \tag{2.2}$$

Here, the models with vector and axial-vector types of mediator are allowed to couple to SM quarks and leptons. There are hence five free parameters: m_{DM}, M_{med},

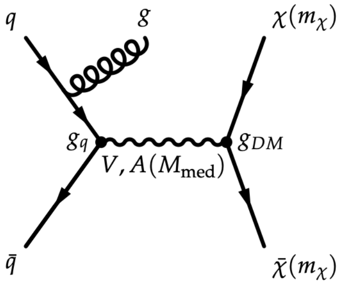

Figure 2.1: Adapted from [21]. Feynman diagram showing DM production via vector and axial-vector mediator with initial state radiation of gluons.

g_{DM}, g_q and g_l. The Feynman diagram illustrating quark anti-quark annihilation with vector and axial-vector models is shown in Figure 2.1. The minimal width of the mediator is the sum of all partial widths for the mediator decaying into quarks and DM. The partial widths for the vector model are given by [19, 21]:

$$\Gamma^{\chi\bar{\chi}}_{vector} = \frac{g^2_{DM} M_{med}}{12\pi}(1 - 4z_{DM})^{1/2}(1 + 2z_{DM}) \tag{2.3}$$

$$\Gamma^{q\bar{q}}_{vector} = \frac{g^2_{q} M_{med}}{4\pi}(1 - 4z_{q})^{1/2}(1 + 2z_{q}) \tag{2.4}$$

$$\Gamma^{l\bar{l}}_{vector} = \frac{g^2_{l} M_{med}}{4\pi}(1 - 4z_{l})^{1/2}(1 + 2z_{l}) \tag{2.5}$$

and for the axial-vector model:

$$\Gamma^{\chi\bar{\chi}}_{axial-vector} = \frac{g^2_{DM} M_{med}}{12\pi}(1 - 4z_{DM})^{3/2} \tag{2.6}$$

$$\Gamma^{q\bar{q}}_{axial-vector} = \frac{g^2_{q} M_{med}}{4\pi}(1 - 4z_{q})^{3/2} \tag{2.7}$$

$$\Gamma^{l\bar{l}}_{axial-vector} = \frac{g^2_{l} M_{med}}{4\pi}(1 - 4z_{l})^{3/2} \tag{2.8}$$

where $z_{DM,q}$ is given by $z_{DM,q} = m_{DM,q}/M_{med}$ and partial width contribution is suppressed when the mass of mediator is less than twice the mass of decay product for given channel.

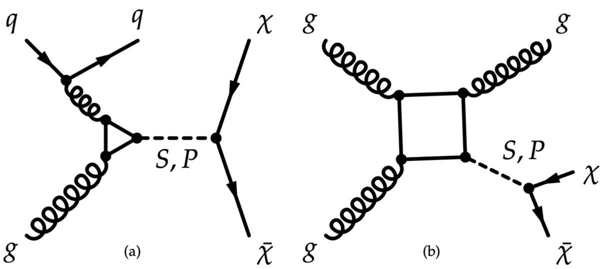

Figure 2.2: Adopted from [21]. One-loop diagrams showing DM production via scalar and pseudo-scalar mediator.

2.2 Pseudo-Scalar model

A spin-0 pseudo-scalar mediator field ϕ is described by the Lagrangian [19, 21]:

$$\mathcal{L}_{pseudo-scalar} = -ig_{DM}\phi\bar{\chi}\gamma_5\chi - ig_q\frac{\phi}{\sqrt{2}}\sum_{q=u,d,s,c,b,t} y_q\bar{q}\gamma_5 q \tag{2.9}$$

This model requires higher energy scales due to the loop-induced mediator production as shown in Figure 2.2. Here, $y_q = \sqrt{2}m_q/v$ are the SM quark Yukawa couplings with $v \simeq 246$ GeV, the Higgs vacuum expectation value. An additional loop-induced decay of mediator into gluons exists. The individual contributions of the total width are [19, 21]:

$$\Gamma^{\chi\bar{\chi}}_{pseudo-scalar} = \frac{g_{DM}^2 M_{med}}{8\pi}(1-4z_{DM}^2)^{1/2} \tag{2.10}$$

$$\Gamma^{q\bar{q}}_{pseudo-scalar} = \frac{3g_q^2 y_q^2 M_{med}}{16\pi}(1-4z_q^2)^{1/2} \tag{2.11}$$

$$\Gamma^{gg}_{pseudo-scalar} = \frac{\alpha_s^2 g_q^2 M_{med}^3}{32\pi^3 v^2} \mid f_{pseudo-scalar}(4z_t) \mid^2 \tag{2.12}$$

and the form factor is:

$$f_{pseudo-scalar}(\tau) = \tau \arctan^2(\frac{1}{\sqrt{\tau-1}}) \tag{2.13}$$

Chapter 3

Dark Matter search methods

Among experiments probing DM, collider experiments aim to detect the production of invisible DM particles as well as the visible decays of the particles mediating such a process [4]. Direct Detection (DD) experiments look for DM-nucleon scattering recoil inside a terrestrial detector [6] and Indirection Detection (ID) experiments look for an excess of SM particles from DM annihilation in the sky [10]. When good agreement is observed between experimental data and Standard Model (SM) predictions, we can interpret the data into exclusion limits in the parameter space of a specific model, as this can help us understand the role of each type of search in the hunt for DM.

3.1 Mono-jet event topology at Colliders

WIMP DM might be produced via $f\bar{f} \rightarrow \chi\bar{\chi}$ processes at colliders. They will be invisible to detectors and can be detected as missing transverse momentum (E_T^{miss}, or MET) at collider experiments. We are not able to look for DM production directly, but instead search for event topologies of E_T^{miss} in association with other particles X. The tracks and energy deposits will be X recoiling against nothing in detectors.

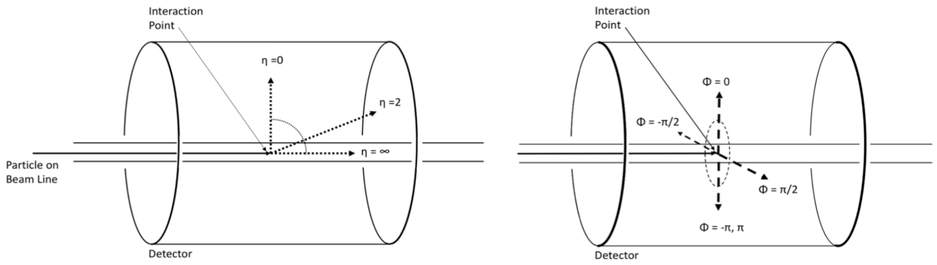

Figure 3.1: Adapted from [22]. Variables describe the momentum of a particle at colliders.

At the Large Hadron Collider (LHC), the collision of partons is likely to produce gluons as initial state radiation. A hadronic jet hence is a natural choice of X as final state, and searches employing that signature are called “mono-jet” meaning an energetic jet in association with E_T^{miss}.

3.1.1 Overview of the mono-jet search

This section overviews the 2016 ATLAS mono-jet search [23], and over the course writing this thesis, a new ATLAS search on mono-jet comes out [24]. Generally speaking, particles deposit energy in calorimeters located at an angle θ relative to the beam line z from their transverse component of velocity. This is how transverse momentum for a jet is reconstructed, which is defined to be $E\sin(\theta)$, where pseudorapidity η is used at the LHC to replace θ:

$$\eta = -\ln(\tan(\frac{\theta}{2})) \tag{3.1}$$

With ϕ defined in the coordinate system, the coordinate system used at LHC experiments is recovered and illustrated in Figure 3.1.

During this search, E_T^{miss} is reconstructed by negative vectorial sum of the energy deposits in the calorimeter of electrons, muons, τ-leptons, photons, and jet up to

$|\eta|= 4.9$ and making use of the tracking information. The analysis selects events with $E_T^{miss} > 250$ GeV.

Jets are reconstructed from energy deposits in the calorimeters using the anti-k_t algorithm [25] with the radius parameter sets to 0.4. The analysis selects events with a maximum of four jets with $p_T > 30$ GeV and $|\eta|< 2.8$. The leading (highest p_T) jet is required to have $p_T > 250$ GeV and $|\eta|< 2.4$. Additional requirements for removing fake jets and jets not belonging to the same proton-proton interactions are imposed.

A separation of $\Delta\phi(jet, E_T^{miss}) > 0.4$ between E_T^{miss} and each selected jet is required to reduce the multijet background. Events with muons identified with $p_T > 10$ GeV or electrons identified with $p_T > 20$ GeV are vetoed in order to suppress the background contributions of W and Z decays.

The above selections identify the signal region for mono-jet analysis, and is further divided into inclusive and exclusive signal regions with varying E_T^{miss} illustrated in Table 3.1 [25]. Three control regions are selected to be kinematically similar to signal region but invert the lepton veto to require one muon, one electron or two muons in the final states [25, 26]. This enriches the background processes of W and Z decays, and are used to normalize and constrain the background estimates in the signal region [26]. As a result, the signal region E_T^{miss} distribution is shown in Figure 3.2.

Inclusive signal region	IM1	IM2	IM3	IM4	IM5	IM6	IM7	IM8	IM9	IM10
$E_T^{miss}(GeV)$	> 250	> 300	> 350	> 400	> 500	> 600	> 700	> 800	> 900	> 1000
Exclusive signal region	EM1	EM2	EM3	EM4	EM5	EM6	EM7	EM8	EM9	EM10
$E_T^{miss}(GeV)$	250-300	300-350	350-400	400-500	500-600	600-700	700-800	800-900	900-1000	> 1000

Table 3.1: Adapted from [23]. Classification of mono-jet signal regions.

3.1.2 Interpreting results to DM model constraints

Since the mono-jet search shows no excess above the SM background, the experimental data as well as the background prediction are interpreted to constrain DM

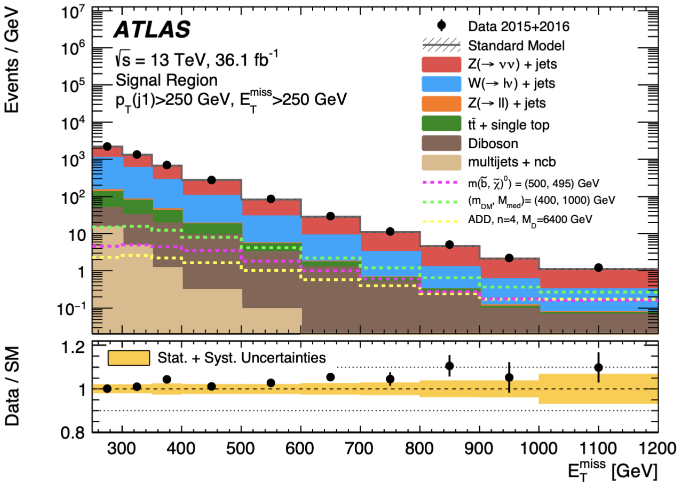

Figure 3.2: Adapted from [23]. MET kinematic distributions from ATLAS.

models. For a model independent limit, only one bin is considered at a time. A simplified version of the likelihood (no systematic uncertainties) reads [26]:

$$\mathcal{L}(\mu, \theta) = P(N|\mu S + \theta B) \times P(N_{CR}|\theta B_{CR}) \tag{3.4}$$

This represents the Poisson probability of observing N and N_{CR} events in the Signal Region (SR) and Control Region (CR), given the total events predicted by the signal plus background hypothesis. Here, μ is the signal strength which scales the predicted number of signal events S, and θ is nuisance parameter scaling the predicted number of background events B or B_{CR}. Given the role of μ, we define:

$$\mu := \frac{\sigma}{\sigma_{theory}} \tag{3.5}$$

σ is the production cross section observed for DM production given experimental data, and σ_{theory} is theory cross section predicted by theoretical models of DM.

The best fit of μ is determined by maximizing the likelihood. The model independent limit is set using the IM regions in Table 3.1. With a similar likelihood encoded in the test statistic and the CL_s method [26], a 95% confidence level upper limit on μ can be obtained. For mono-jet model independent limit, there is no need to know S and emphasize μ, since only one term in the likelihood involves S as shown in equation 3.2. Therefore, the product, $\mu^{95,CL}S$, will always appear together as the maximum events number signal can have for corresponding IM region. Dividing the number of events constrained by the model independent limit over collision luminosity, we obtain the limit on visible cross section. Mono-jet model independent limits are summarized in Table 3.2.

Selection	$\langle\sigma\rangle_{obs}^{95}$	S_{obs}^{95}	S_{exp}^{95}
IM1	531	19135	11700^{+4400}_{-3300}
IM2	330	11903	7000^{+2600}_{-2600}
IM3	188	6771	4000^{+1400}_{-1100}
IM4	93	3344	2100^{+770}_{-590}
IM5	43	1546	770^{+280}_{-220}
IM6	19	696	360^{+130}_{-100}
IM7	7.7	276	204^{+74}_{-57}
IM8	4.9	178	126^{+47}_{-35}
IM9	2.2	79	76^{+29}_{-21}
IM10	1.6	59	56^{+21}_{-16}

Table 3.2: Adapted from [23]. Mono-jet 95% CL model independent limits.

The mono-jet model dependent limit includes all EM regions, and is done using a fit to the E_T^{miss} distribution. The limit is model dependent in the sense that it takes account of the shape information of E_T^{miss} for each signal hypothesis. The simplified version of this joint-likelihood (no systematic uncertainties) reads [26]:

$$\mathcal{L}(\mu, \theta_k) = \prod_b P(N_b|\mu S_b + \sum_k \theta_{kb} B_{kb}) \times \prod_{l,b} P(N_{lb}|\sum_k \theta_{kb} B_{klb}) \tag{3.6}$$

where b counts over bins of E_T^{miss}, k counts over background events and l counts over the control regions.

Using the CL_s method, the upper limit on μ is obtained, and the model is excluded if it is smaller than one. The result for the AV model is shown in Figure 3.3 as a function of mediator and DM mass. The exclusion contour shows that for model with an axial-vector mediator exchange, the sensitivity of mono-jet analysis increases when the dark matter and mediator masses decrease, and when $M_{med} > 2m_\chi$. Here, if two

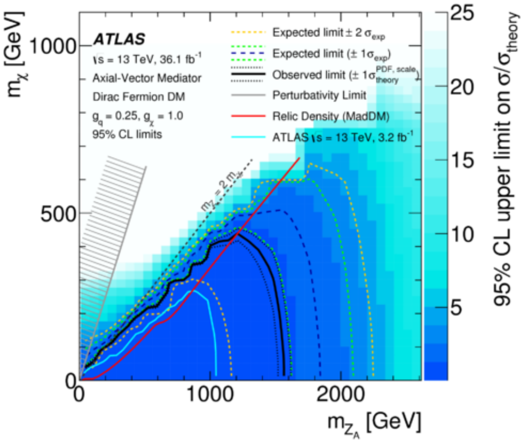

Figure 3.3: Adapted from [23]. Mono-jet 95% CL signal strength for axial-vector model.

points on DM model parameter space have same shape for E_T^{miss} distribution, μS_b in equation 3.4 won't change after scaling μ by the ratio of cross section.

3.2 Di-jet event topology at Colliders

If DM will be produced in proton-proton collisions at the LHC via a mediator with sizable couplings to quarks, the SM decays of such mediating particles should also be visible as a two-jet resonance. This will result in a local excess in the smooth di-jet invariant mass (m_{jj}) background distribution from QCD. If no excess is found, the m_{jj}

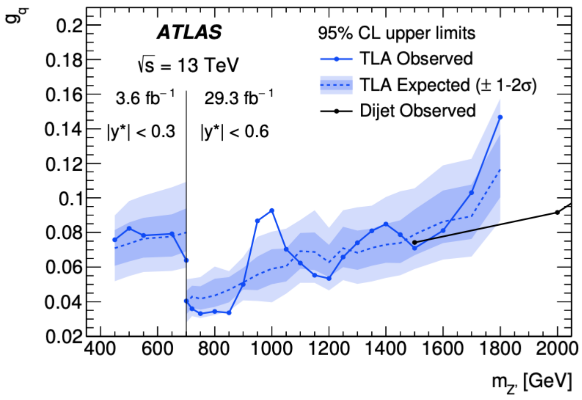

Figure 3.4: Adapted from [27]. TLA di-jet 95% CL upper limits on g_q.

distribution observed can hence help set upper limits on values of the quark-mediator coupling constant with respect to mediator mass. These are also the parameters that describe the SM mediator decay process together with the DM mass versus mediator mass as in mono-jet case. The details on a di-jet analysis searching for DM mediators can be found in [27, 28].

As an example, Figure 3.4 shows the di-jet trigger-object-level analysis (TLA) approach [27] that reaches mediator masses below 1 TeV. Solid and dashed lines represent observed and expected limits, obtained in a similar way to those in mono-jet case. The limits are first set in terms of visible cross section where the branching ratio B $(Z^{'} \rightarrow \text{SM})$ and acceptance A are both incorporated in $\sigma_{visible}$ calculation. The limits then are transferred to the $(g_q, m_{Z'})$ plane under the axial-vector simplified model. The branching ratio of $Z^{'}$ to DM is assumed to be negligible during the signal generation process, but adding DM decays would not significantly change the picture.

3.3 Indirect Detection

The annihilation products of DM interactions can result in γ-rays and can be observed either directly or from subsequent electromagnetic showering. Some DM Indirect Detection (ID) experiments aim to detect those gamma-rays with a γ-ray telescope [7] or by recording $e^{+}e^{-}$ pairs on Earth [8]. The observation of no excess consistent with DM is then interpreted in terms of upper limits on DM annihilation cross section using the CL_s method. In presenting the results, specific DM annihilation channels are assumed, and the branching ratio to other channels set to zero.

Figure 3.5 (right) shows the Feynman diagram for DM ID. The gamma-ray signal flux at the Fermi Large Area Telescope (LAT) [9, 10] relates to the DM annihilation

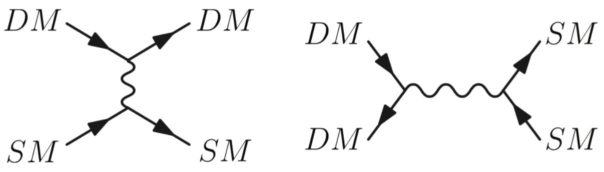

Figure 3.5: Diagram for direct detection (left) and indirect detection (right).

cross section by [9, 10]:

$$\Phi_s(\Delta\Omega) = \frac{1}{4\pi}\frac{\langle\sigma v\rangle}{2m_{DM}^2}\int_{E_{min}}^{E_{max}}\frac{dN_\gamma}{dE_\gamma}\,dE_\gamma \times \int_{\Delta\Omega}\int_{l.o.s.}\rho_{DM}^2(\mathbf{r})\,dl d\Omega' \tag{3.7}$$

where $\langle\sigma v\rangle$ is the thermal average annihilation cross section and m_{DM} is the dark matter mass. The first integration counts the number of gamma rays as signal yield in the experimental energy range. The second integration is know as the J-factor, which is the line-of-sight integral through the DM distribution over a solid angle $\Delta\Omega$.

Figure 3.6 is part of the 2015 Fermi results [9] searching for DM annihilation from 15 Milky Way Dwarf Spheroidal Galaxies (dSph). The analysis assumed a double power-law structure cusp profile of DM taking into account the large uncertainties of corresponding 15 J-factors by maximizing the joint-likelihood. The solid line shows the observed limit and the dashed line shows the expected limit. The green and yellow bands indicate 68% and 95% confidence level ranges for the expected limit.

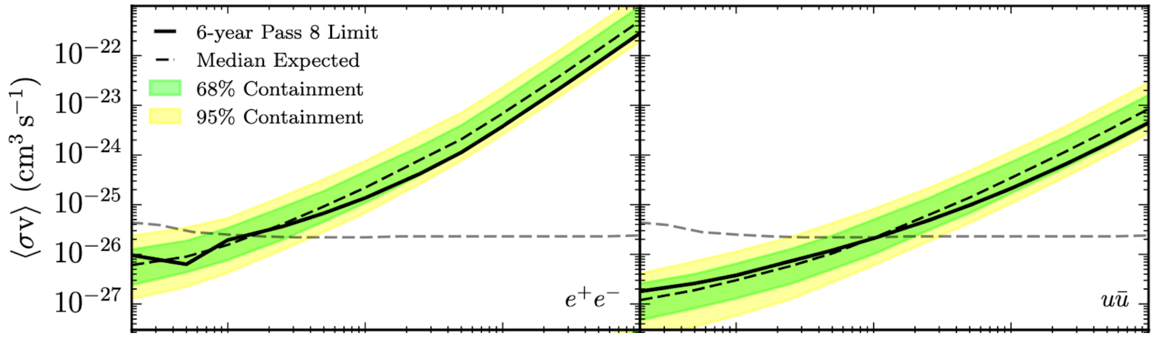

Figure 3.6: Adapted from [9]. The 95% CL DM annihilation cross section upper observed limits for various channels has been assumed.

3.4 Direct Detection

If our galaxy is embedded in a halo of DM, then DM should pass through Earth's surface [6]. Detecting DM-nucleon scattering on Earth is known as DM Direct Detection (DD) experiments and are mostly underground to suppress cosmic ray backgrounds. A diagram for DM DD is shown in Figure 3.6 (left). A signal of WIMP DM appears as a recoiling nucleus in a detector. In absence of any signal, one can set limits on DM-nucleon scattering cross section.

Here, vector or scalar mediators would lead to a spin independent (SI) interaction while axial-vector or pseudo-scalar mediator would lead to a spin dependent (SD) interaction. A SI interaction assumes DM-proton and DM-neutron to have equal cross section and SD interaction does not. Current experiments have different target nucleon and detection technology. For SI interaction, two phase Xenon experiments such as LUX [29] and XENON1T [30] can detect heavier DM for m_{DM} approximately greater than 10 GeV, while solid state cryogenic detectors such as SuperCDMS [31] and CRESST II [32] are more sensitive than Xenon detectors in lower mass range due to their lower energy threshold. DD sensitivities for SI DM-nucleon interaction are illustrated in Figure 3.7 (left panel) and for SD interaction is summarized in Figure 3.7 (right panel).

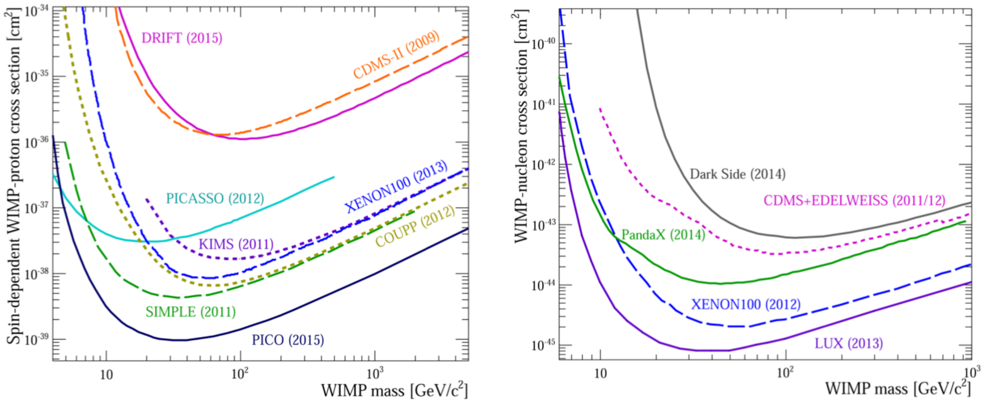

Figure 3.7: Adapted from [6]. Upper limits for for SD DM-nucleon cross section assuming pure proton coupling (left), and SI DM-nucleon cross section (right).

Chapter 4

Presentation of Collider results together with model-dependent Indirect Detection

This chapter studies the dark matter ID bounds and translates future collider results in simplified models for Dirac DM exchanging a pseudo-scalar mediator with quarks through the s-channel. The most important features of different annihilation channels are studied as well. During this study, I found that the mapping from the collider exclusion plane to the ID plane is not purely one to one due to the resonance of Dark Matter annihilation. This reduces the exclusion range when translating collider limits on Dark Matter to the ID plane. While focusing on s-channel pseudo-scalar mediator here, this problem also occurs in some models with other types of mediator, such as axial-vector DM simplified model.

4.1 Translation

I translate the projected limits on the DM production cross section in mono-jet to limits on $\langle \sigma v_{rel} \rangle$ for three future colliders: HL-LHC (14 TeV 3 ab^{-1}), HE-LC (27

TeV 15 ab^{-1}) [33] and FCC-hh (100 TeV 100 ab^{-1}) FCC for a Dirac pseudo-scalar mediator model. The translated collider limits and ID limits are all at 95% CL. The assumption made for collider experiments is that DM will interact with all flavor of quarks, hence the collider limits will be translated to the ID plane through the sum of annihilation cross sections over all quark flavors and gluons. The mediator couplings to DM and quarks are both set to 1.0. In [19], the annihilation cross sections for quarks is given by:

$$\langle \sigma v_{rel} \rangle_q = \frac{3m_q^2}{2\pi v^2} \frac{g_q^2 g_{DM}^2 m_{DM}^2 \sqrt{1 - \frac{m_q^2}{m_{DM}^2}}}{(M_{med}^2 - 4m_{DM}^2)^2 + M_{med}^2 \Gamma_{med}^2} \tag{4.1}$$

and for gluons:

$$\langle \sigma v_{rel} \rangle_g = \frac{\alpha_s^2}{2\pi^3 v^2} \frac{g_q^2 g_{DM}^2 \mid \sum_q m_q^2 f(\frac{m_q^2}{m_\chi^2}) \mid^2}{(M_{med}^2 - 4m_{DM}^2)^2 + M_{med}^2 \Gamma_{med}^2} \tag{4.2}$$

where m_{DM}, M_{med}, g_{DM} and g_q are free model parameters as introduced in Chapter 2. Γ_{med} is the total width of the pseudo-scalar mediator and f is the form factor defined in equation 2.13. The shape of translated collider limits in DM mass-$\langle \sigma v_{rel} \rangle$ plane is given by channels of six quarks and gluons. The top quark channel turns on at $m_{DM} = m_{top}$ GeV which appears as a jump of limit in Figure 4.1.

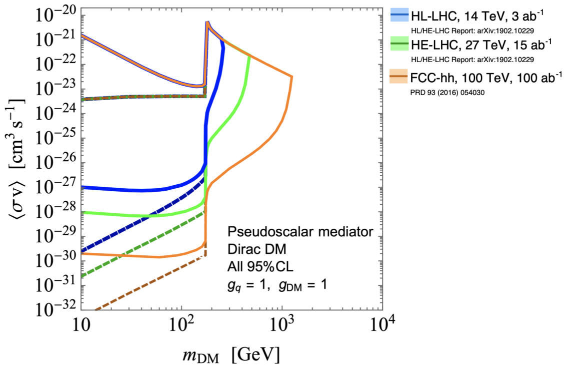

Figure 4.1: Comparison of total annihilation cross section with and without gluons. The total annihilation cross sections without gluons are shown as dashed lines.

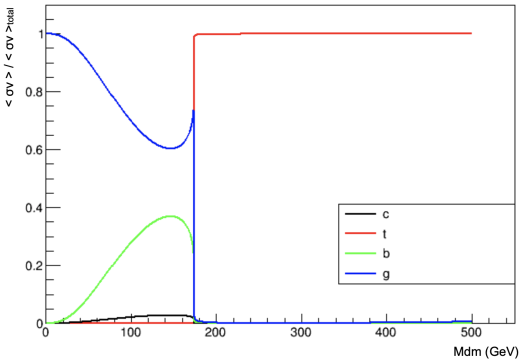

Figure 4.2: Partial annihilation rates of four major DM annihilation channels for DM pseudo-scalar simplified models.

The dashed, darker lines are cases only considering contributions from quarks. The limits here are obtained via translating the boundary lines in future collider exclusion contours. Other channels are no longer important as their contribution to the total $\langle \sigma v_{rel} \rangle$ will be small compared to the top quark after it turns on. In Figure 4.2, the partial annihilation rates of four major channels are shown and we can see the gluons' channel is important before the top quark channel turns on but is negligible afterwards.

In collider searches, there is an entire area of excluded points to translate from the DM-mediator mass plane to the ID plane, not only a contour. In some cases, a point in the mass-$\langle \sigma v_{rel} \rangle$ plane maps to two points in mass-mass plane, due to the resonance of DM annihilation. Not all of the mass-mass plane points are excluded by colliders as, for example, in Figure 4.3. The marked points in the right panel represent two points that give the same value of annihilation cross section, but have different mediator masses in the left panel. This will cause the contour-only translation method to become invalid once only one mediator mass point falls in the contour, while the other is not excluded. In other words, we can't completely exclude the corresponding point in the ID plane, given this point maps to an excluded point and an un-excluded point in the mass-mass plane.

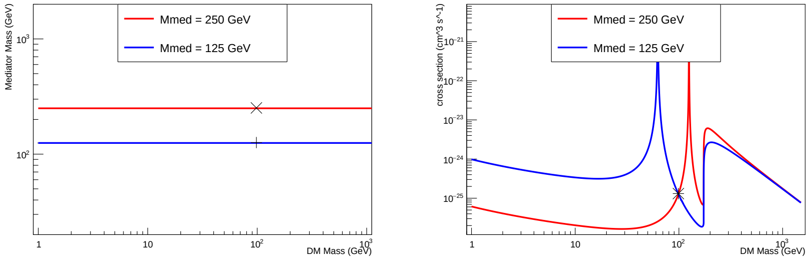

Figure 4.3: Translate points of constant mediator mass in mass-mass plane with a pseudo-scalar assumption using equation 4.1 and 4.2.

Therefore, a study on mapping topology is conducted as shown in Figure 4.4. As a result, the above problem will only occur above a certain benchmark line in the mass-$\langle \sigma v_{rel} \rangle$ plane. To illustrate this, I translated straight lines with constant mediator mass in the mass-mass plane to the ID plane. From studying the resulting mapping behavior in Figure 4.4, I conclude that the translated line with mediator value which goes to zero can serve as a benchmark line, and the region below that benchmark line is the valid area where the collider result excludes all the possibilities. Only in this region can points in the mass-$\langle \sigma v_{rel} \rangle$ plane map to a single point in mass-mass plane and vice versa.

In Figure 4.5, I modified figure that I contributed to [35], where I translated future collider limits to ID results: Fermi ($b\bar{b}$ only) [10], HESS ($b\bar{b}$ only, projected constraints) [36], CTA GC ($b\bar{b}$ only, projected constraints) [37] and Fermi+LSST ($b\bar{b}$

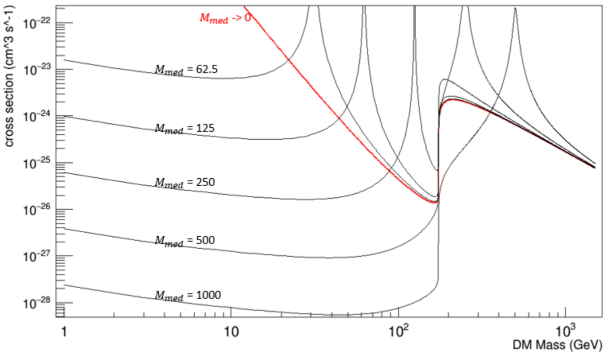

Figure 4.4: Translate lines with constant mediator mass in mass-mass plane with a pseudo-scalar assumption using equation 4.1 and 4.2.

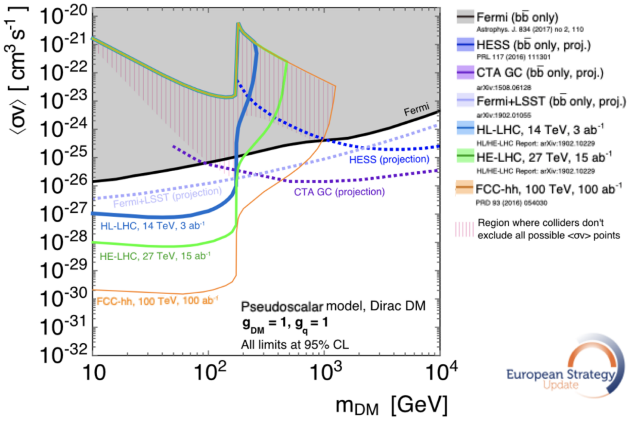

Figure 4.5: Modified from [35]. Comparison of translated future collider results to the ID limits. The collider limits are for pseudo-scalar mediator with $g_q = 1$, $g_{DM} = 1$. All limits are at 95% CL. The shaded region is where collider doesn't exclude all the possibilities.

only, projected constraints) [38]. The cross sections of all the ID results are multiplied by a factor of two in order to convert $\langle \sigma v_{rel} \rangle$ from Majorana DM in original ID results to the Dirac DM scenario to match the DM assumption in collider experiments. The shaded region is where the collider result excludes some but not all of the possibilities.

4.2 Joint Dark Matter annihilation channels

Working with Prof. Linda Carpenter, I adapted code she originally used to produce figure 2 for an earlier publication [39] to scan over dark matter mass while statistically reproducing the Fermi dark matter annihilation cross section upper limit. With this code, I studied how model-dependent DM simplified pseudo-scalar model dark matter annihilation constraints differ from those of the single $b\bar{b}$ channel.

The model-dependent constraints are obtained first by calculating the annihilation cross section for each channel of the model. To achieve this, I use MadDM [40] for a numerical computation. These are then converted into branching ratios with respect to the total DM annihilation cross section. The electromagnetic showering and the corresponding gamma ray spectrum for each channel at the production point at given

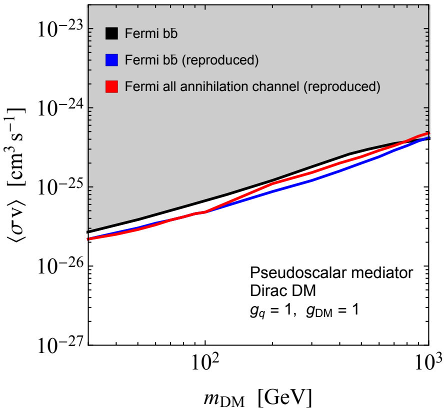

Figure 4.6: Reproduced Fermi limit (red and blue lines) compared with Fermi published result [9]. The reproduced limits and Fermi limit are all at 95% CL.

DM mass is calculated using PPPC 4DMID [11]. These are then combined by scaling the energy of corresponding spectrum by its branching ratio and taking the sum for every channels. I adapted J-factors from Martinez et al. [41], which then are used to calculate the combined-channel flux at earth. For each dwarf spherical galaxy, I used the 2016 flux-likelihood table for a total of 24 bins. The tables then are fit with a quadratic model, and the resulting fit functions are used to find the likelihood corresponding to all-annihilation-channel flux at the production point. Due to the large uncertainty of J-factors, the best fit values are found and adapted in the analysis by maximizing the joint-log-likelihood for dwarf spherical galaxies. For a single DM mass point, I tested multiple cross section values and output corresponding likelihoods and best fit J-factors. The one that is closest to 95% CL value is picked as the all-annihilation-channel upper limit.

The result is shown in Figure 4.6, which assumes DM annihilating into all types of quarks and charged leptons for the pseudo-scalar model. There are no major differences between the reproduced all-annihilation-channel Fermi limit, the reproduced $b\bar{b}$ Fermi limit, and the $b\bar{b}$ Fermi published results. Therefore, I only show $b\bar{b}$ Fermi published results during the DM ID and collider comparison.

Chapter 5

Outlook: low g_q Dark Matter summary plots

Plots summarizing the constraints on Dark Matter models can help visualize the complementarity between different searches for the same kind of experiment, as well as between different experiments. As in Figure 5.1 [42], exclusion comparisons in the DM mass – mediator mass plane (left panel) combine searches for both invisible and visible signals of the model, while plots on mediator – quark coupling and mediator mass plane (right panel) show the production couplings as a function of the mediator mass in and visible decay of the mediator.

We can also compare collider searches together with present and future ID and DD experiments, using variables commonly employed by displaying indirect and direct detection results with the methods recommended by the LHC DM WG [19]. An example of such plots using fixed mediator – quark couplings is shown in Figure 5.2 [35].

So far, the presentation of LHC results as well as the presentation of projections of future hadron collider experiments have focused on four benchmark scenarios with different choices of couplings to quarks and leptons, as recommended by the Dark

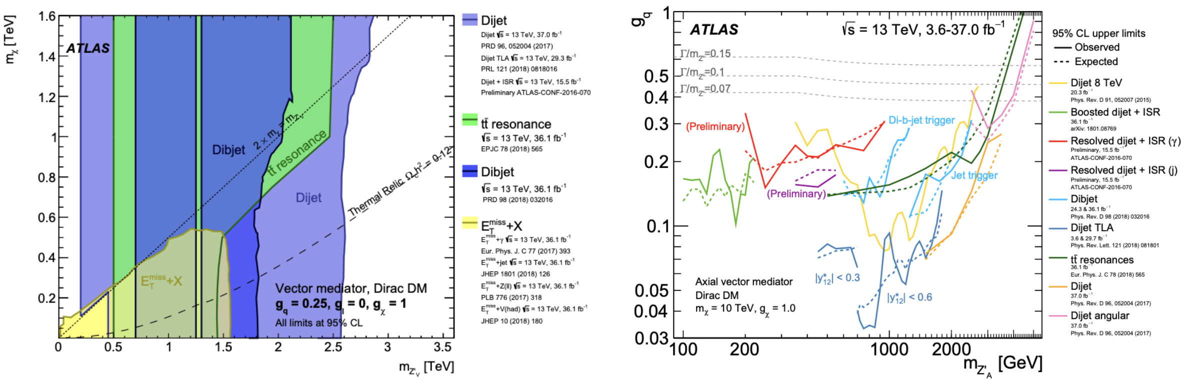

Figure 5.1: Left: regions in DM mass - mediator mass plane excluded at 95% CL by visible and invisible searches. Right: different dijet search contours for 95% CL upper limits on the coupling g_q as a function of resonance mass $m_{Z'_A}$. All adapted from [42].

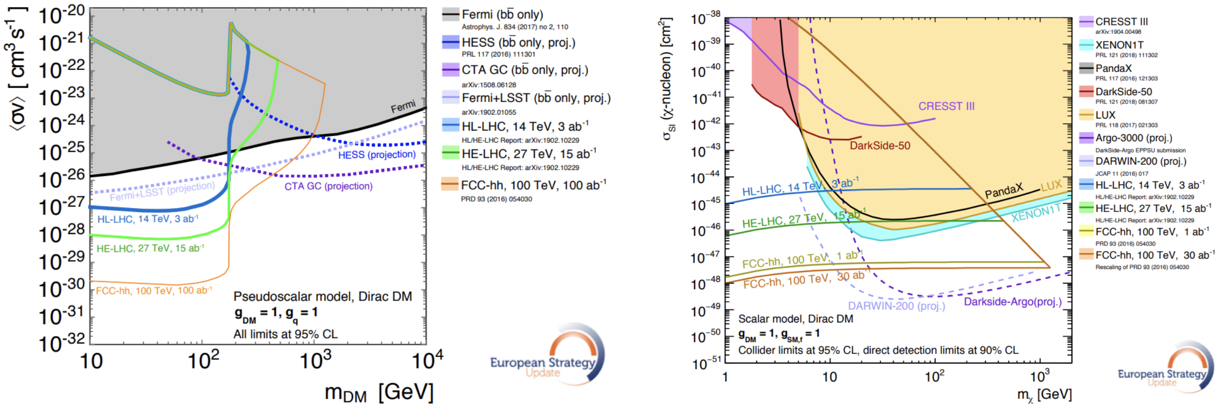

Figure 5.2: Left: projected limits from future colliders with constraints from current and future ID experiments at 95% CL. Right: 95% CL projected limits from future colliders with constraints from current and future DD experiments on the spin-independent DM–nucleon scattering at 90% CL. All panels adapted from [35].

Matter Working Group (DM WG) [20]. Using the methods from my ongoing work in synergy between the LHC DM WG and the Snowmass community [43] on collider limits with lower mediator - quark coupling values has several advantages over the fixed coupling values proposed by the LHC DM WG and adopted in the European Strategy Briefing Book [35]. This will allow us to have a more complete picture of the complementarity of collider DM searches with direct and indirect detection, as well as compare collider results with collaborations that are sensitive to much lower couplings, such as accelerator-based and fixed target experiments.

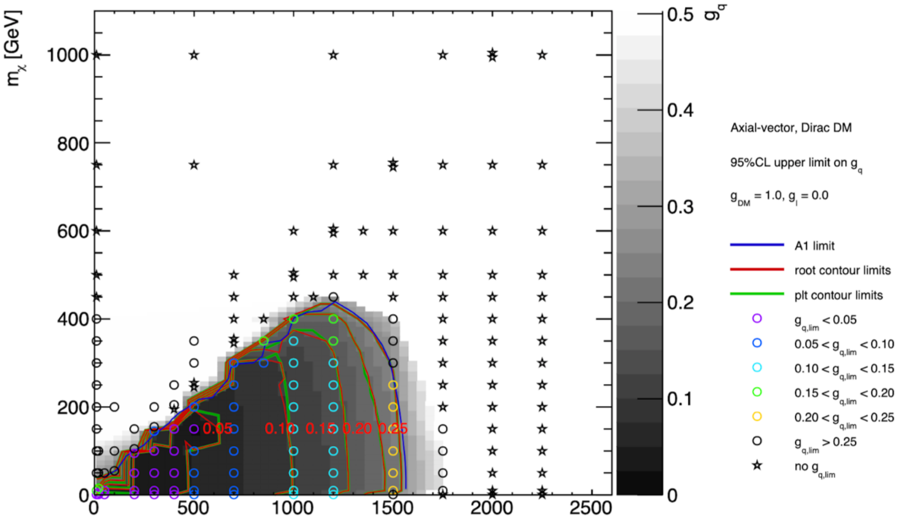

Figure 5.3: Upper g_q limits for axial-vector model using method from [43]. Here, $g_{DM} = 1.0$ and $g_l = 0.0$. Interpolation contours for different g_q values are indicated in red (by ROOT) and green (by Matplotlib). The limits are at 95% CL.

5.1 Comparison of dark matter experimental exclusions in the low g_q regime

The upper limits on couplings to quarks can be used for illustrating the exclusions of the mono-jet analysis. This can exhibit exclusions of multiple g_q values in the same figure. The upper limit on g_q for a model point is found by looping on the coupling values and scaling the corresponding signal strength limit until $\mu_{lim} = 1.0$. The upper g_q limits on axial-vector and vector models can be found using the 2016 mono-jet analysis [23], which published data on the axial-vector model. My upper g_q limit results for the axial-vector model are shown in Figure 5.3 as an example, where model points that don't have an upper limit on g_q are indicated as stars. We can see the interpolated contour at $g_q = 0.25$ fits the original ATLAS result [23]. The red or green contours can be regarded as 95% CL limits on the model at the corresponding g_q choice. The direct translation of the signal strength limits in terms of different coupling values in the mass-mass plane, and compared to di-jet searches, is shown in Figure 5.4.

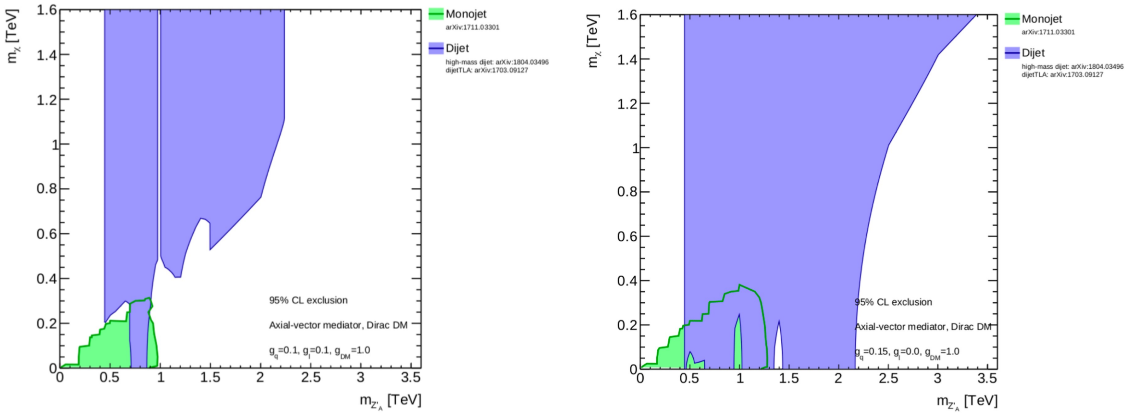

Figure 5.4: $g_q = 0.10$ (left) and $g_q = 0.15$ (right) limits on high-mass di-jet [28], di-jet TLA [27] and ATLAS mono-jet [23] using method from [43]. The limits are at 95% CL.

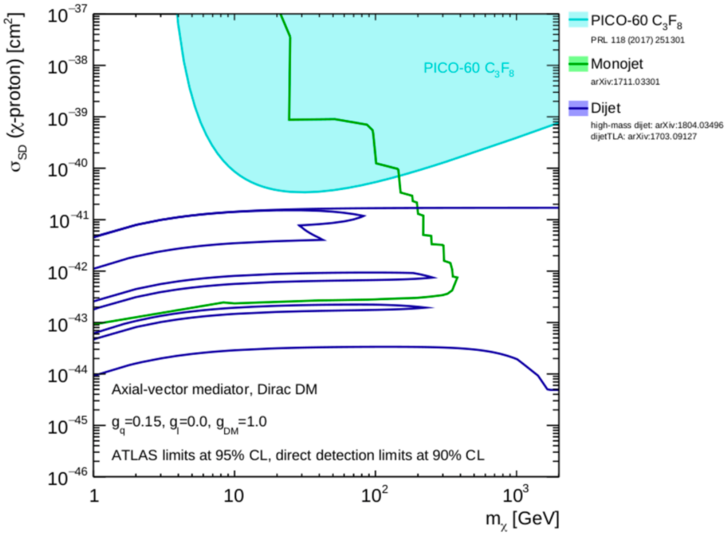

Figure 5.5: Comparing the PICO-60 C_3F_8 DM DD experiment [44] with low g_q exclusion contours from this work.

I also translated the exclusion contours in Figure 5.4 (right panel) using equation (4.10) from [19] to values for DM-nucleon scattering, then compared with the PICO-60 C_3F_8 DM DD experiment [44]. The result is illustrated in Figure 5.5.

Chapter 6

Mono-jet Monte Carlo signal generation framework

While translating the limits to lower g_q, we find that the results for the discrete model points in Ref. [23] are too coarse and can no longer handle the translation for $g_q < 0.05$ as illustrated in Figure 6.1. Given that this problem occurs in the mono-jet translation, it is necessary to build a Monte Carlo (MC) signal generation framework for the mono-jet and compare those signal distributions in the low DM mass, mediator mass regime for the model of interest to see whether the shapes of the signal distribution remain the same and therefore can be easily reinterpreted. The 13 TeV center of mass collision energy of the LHC should be in principle large enough for points in this regime to have the same signal distribution, hence their signal strengths can be further interpreted using the ratio of cross section as described in Chapter 3.1.2.

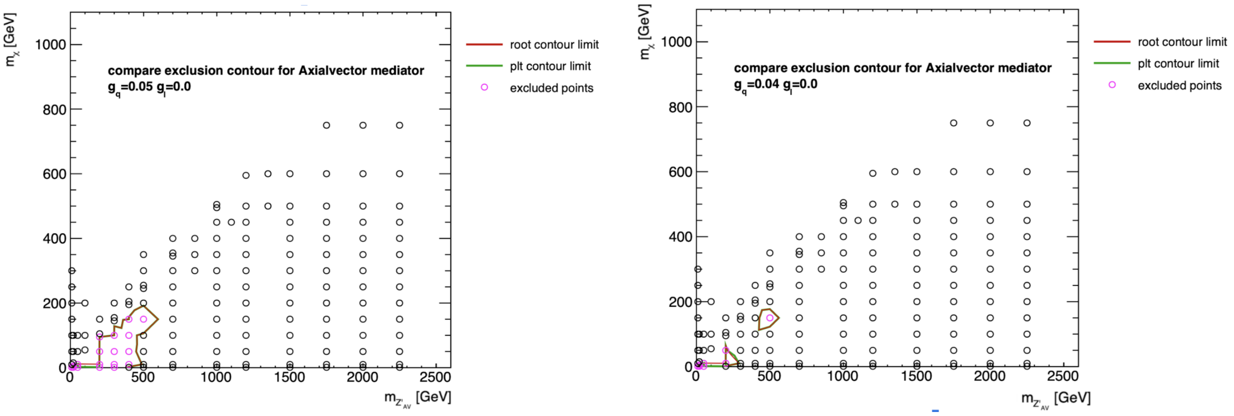

Figure 6.1: Translate mono-jet signal strength from $g_q = 0.25$ to $g_q = 0.05$ (left) and $g_q = 0.04$ (right) using the method from [43].

6.1 Short description of the framework

This mono-jet Monte Carlo signal generation framework is only for truth level as illustrated in Figure 6.2 where no detector effect is simulated. Therefore, the following analysis won't address cuts on event cleaning, jet quality, etc.

I use MadGraph5_aMC@NLO [46] for event generation at the Leading Order (LO) accuracy. During this process, I find that the mediator width of the model has to be set manually in the parameter card. Events are generated using NNPDF23LO [47] PDFs. Since a phenomenological model like Pythia may reproduce data better than fixed multiplicity event generation, the 1-jet scenario with dark matter production is first generated. The corresponding Feynman diagram is shown in Figure 2.1. Here, higher jet multiplicities are accomplished all by Pythia8 [48] event showering where

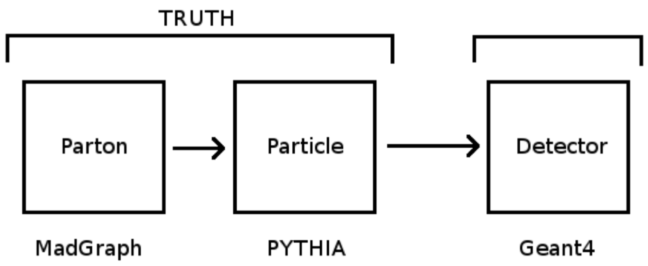

Figure 6.2: Adapted from [45]. Schematic illustration for different steps of simulation.

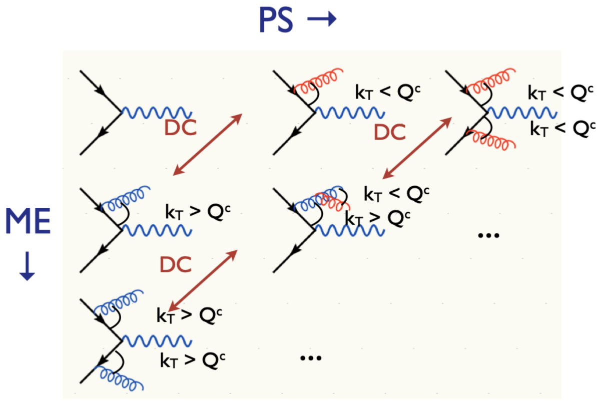

Figure 6.3: Adapted from [51]. Illustration of Double Counting between higher multiplicity Matrix Element (ME) generation and subsequent Parton Showering (PS).

radiation, gluon splitting and hadronization are computed. In my analysis, MadAnalysis5 [49] is used to process the parton level result and Rivet [50] is used to process the hadron level result. The corresponding event selection cuts are coded in Rivet [50] following the 2020 ATLAS mono-jet analysis [24]. The resulting parton level kinematic distributions of mediator, event selection cut flow, and hadron level kinematic distribution of missing transverse momentum for models in Chapter 2.1 are validated with results from different publications in the next section.

Alternatively, two processes' event generation for 1 and 2 jet multiplicities with dark matter production are generated and combined using the MLM merging algorithm [52] during the showering process. A vetoing procedure is conducted during merging in order to avoid doubling counting of the same jet multiplicity scenario as illustrated in Figure 6.3. The resulting events are then processed by Rivet and the kinematic distributions of missing transverse momentum for different merging scales are addressed as well.

6.2 Validation plots and cut flow comparison

The parton level validation of the framework is the first step to test the model in terms of Universal FeynRules Output (UFO) adapted from the feynrules website [53], the mediator width calculation, as well as the Madgraph run card and process card settings. I plot the two-particle dark matter invariant mass distributions with varying couplings for vector model parton result as shown in Figure 6.4 top panel. These set of plots agree with those shown in figure 2.5 top panel of the LHC dark matter forum [21]. The parton level MET distribution shapes with varying couplings are also plotted, which in principle should depend mostly on the mediator mass rather than on the couplings, as mediator is what the Initial State Radiation (ISR) jet recoils against. My result in Figure 6.4 bottom panel doesn't change in shape, hence confirms this prediction.

The hadron level validation of the framework is necessary to test the Rivet analysis I coded following the 2020 ATLAS mono-jet analysis benchmark [24] and the Mad-

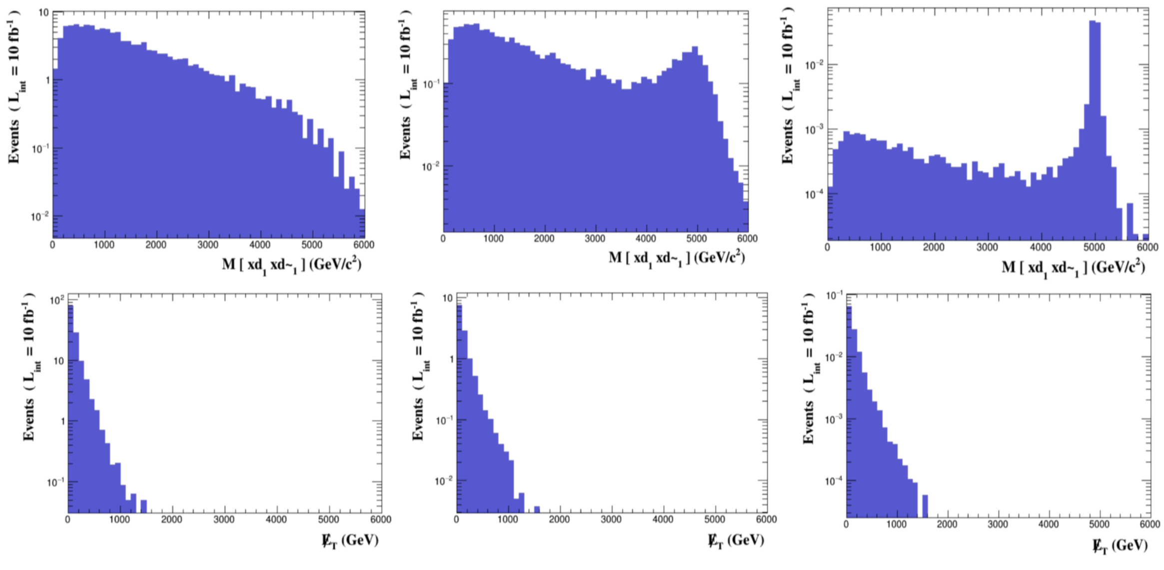

Figure 6.4: Parton level dark matter invariant mass (top) and MET (bottom) distribution for vector model with $m_\chi = 10$ GeV and $M_{med} = 5$ TeV by MadAnalysis5 [49]. From left to right, the coupling choices are $g_{DM} = g_{SM} = 1.0$, $g_{DM} = g_{SM} = 0.5$ and $g_{DM} = g_{SM} = 0.1$. The mediator coupling to SM doesn't include those with leptons.

Name	Description	Rivet implementation
Jet reconstruction	• Anti-k_t algorithm with $R = 0.4$ Calorimeter covers the pseudorapidity range $\lvert\eta\rvert< 4.9$ • Jets with pT > 20GeV and $\lvert\eta\rvert< 2.8$ are considered in the analysis • Discard jets if separation $\Delta R_{j,e}$ is less than 0.2 Discard jets with pT > 30GeV and < 3 tracks with pT > 500MeV, if $\Delta R_{j,\mu}$ is less than 0.4	• FastJets jets(FinalState(Cuts::abseta < 4.9), FastJets::ANTIKT, 0.4); • const Jets jets = apply⟨JetAlg⟩(event, “Jets”).jetsByPt(Cuts::pT > 20*GeV && Cuts::abseta < 2.8); • const Jets isojets = filter_discard(jets, [&](const Jet& j) {if (any(elecs, deltaRLess(j, 0.2))) return true; if (j.pT() > 30*GeV && j.particles(Cuts::pT > 0.5*GeV).size() < 3 && any(mus, deltaRLess(j, 0.4))) return true;});
Electron reconstruction	• Required to have pT > 7GeV and $\lvert\eta\rvert< 2.47$ • Remove electrons separated by ΔR, between 0.2 and 0.4 from any remaining jet	• FinalState electrons(Cuts::abspid == PID::ELECTRON && Cuts::abseta < 2.47 && Cuts::pT > 7*GeV); • const Particles isoelecs = filter_discard(elecs, [&](const Particle& e) {for (const Jet& j : isojets) {if (deltaR(j,e) > 0.2 && deltaR(j,e) < 0.4) return true;} return false;});
Muon reconstruction	• Required to have pT > 7GeV and $\lvert\eta\rvert< 2.5$ • Discard muon if it is matched to a jet with pT > 30GeV, that has at least three tracks associated with it	• FinalState muons(Cuts::abspid == PID::MUON && Cuts::abseta < 2.50 && Cuts::pT > 7*GeV); • const Particles isomus = filter_discard(mus, [&](const Particle& m) {for (const Jet& j : isojets) {if (deltaR(j,m) > 0.4) continue; if (j.pT() > 30*GeV && j.particles().size() > 3) return true;} return false;});
MET reconstruction	• Reconstructed from negative vectorial sum of the transverse momenta of electrons, muons, τ leptons, photons, and jets with pT > 20GeV and $\lvert\eta\rvert< 4.9$	• VisibleFinalState calofs(Cuts::abseta < 4.5 && Cuts::pT > 20*GeV); • MissingMomentum met(calofs); • const Vector3& vet = apply⟨SmearedMET⟩(event, ”MET”).vectorEt(); • const double etmiss = vet.perp();
First MET p_T cut	p_T > 150GeV	if (etmiss < 150*GeV) vetoEvent;
Lepton veto	Veto event with lepton in the final state	if (!isoelecs.empty() || !isomus.empty()) vetoEvent;
Number of jets	Require up to four jets in the final state	if (isojets.size() > 4) vetoEvent;
Azimuthal separation	Greater than 0.4 between MET direction and jets	if (any(isojets, deltaPhiLess(-vet, 0.4))) vetoEvent;
Leading jet p_T, η	$p_T > 150GeV$, $\lvert\eta\rvert< 2.4$	if (filter_select(isojets, Cuts::pT > 150*GeV && Cuts::abseta < 2.4).empty()) vetoEvent;
Second MET p_T cut	p_T > 200GeV	if (etmiss < 200*GeV) vetoEvent;

Table 6.1: Truth level mono-jet event reconstruction and event selection given in Ref. [24] and implemented in my Rivet analysis.

graph pythia card for merging. Truth level procedures given in the ATLAS mono-jet paper and considered in my corresponding Rivet analysis are illustrated in Table 6.1. The first four rows are event reconstruction, including event reconstruction level cuts, requirements on existing leptons and jets, as well as jet algorithm. The following six rows are event selection cuts. The corresponding cut flow for my single jet multiplicity scenario with showering, and comparison with ATLAS cut flow for the same model, is shown in Table 6.1.

My cut flow on leading jet p_T and η isn't in complete agreement compared with the ATLAS cut flow since the latter is at Next-to-Leading Order (NLO) in the strong

Name	$N_{evts}^{1process}$ (framework)	$percent_{evts}^{1process}$ (framework)	$percent_{evts}$ (ATLAS)
After evt cleaning ($p_T^{MET} > 150$GeV)	3867	100%	98.14%
Lepton veto	3756	97.13%	95.19%
Number of jets	3276	84.72%	91.95%
Azimuthal separation	2922	75.56%	88.54%
Leading jet quality	N/A	N/A	87.17%
Leading jet p_T, η	2899	74.97%	64.60%
MET p_T 200GeV	2092	54.10%	51.71%

Table 6.2: Cut flow comparison for my LO truth level one jet process plus showering with ATLAS NLO reconstruction level results. Model here is for axial vector mediator s-channel exchange with $m_\chi = 1$GeV, $M_{med} = 2000$GeV, $g_q = 0.25$, $g_{DM} = 1.0$.

coupling constant, and includes detector effects. However, a reasonable agreement is obtained after the 250 GeV MET cut.

The resulting bin distribution for EM regions (classified in Table 3.2) is shown in Figure 6.5 left panel. Here, the dotted line is an overall k-factor of 2.1 reported by José Zurita, Víctor Lozano and Rosa Seoane in a presentation at CERN [54]. The result I obtained is mostly consistent with this ratio. The distributions for 1 and 2 jets processes with varying MLM merging scale (xqcut) are shown in Figure 6.5 right panel. This result doesn't fit in with the shape of ATLAS mono-jet analysis well, compared with the single jet process.

Different merging parameters are tested for sub-leading jet distributions in terms of 1 and 2 jets processes. The results are shown in Figure 6.6, where the xqcut = 10 GeV choice is shown in the left panel and xqcut = 12 GeV choice is shown in the right panel. From the shape comparison between the sub-leading jet distributions,

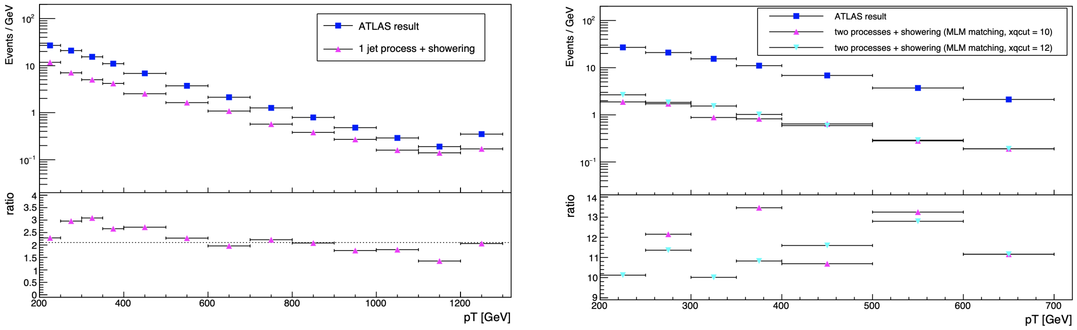

Figure 6.5: Kinematic distributions for model in Table 6.1. The 1 jet process (left panel) and 1 plus 2 jets processes (right panel) are plotted with their ratio to ATLAS.

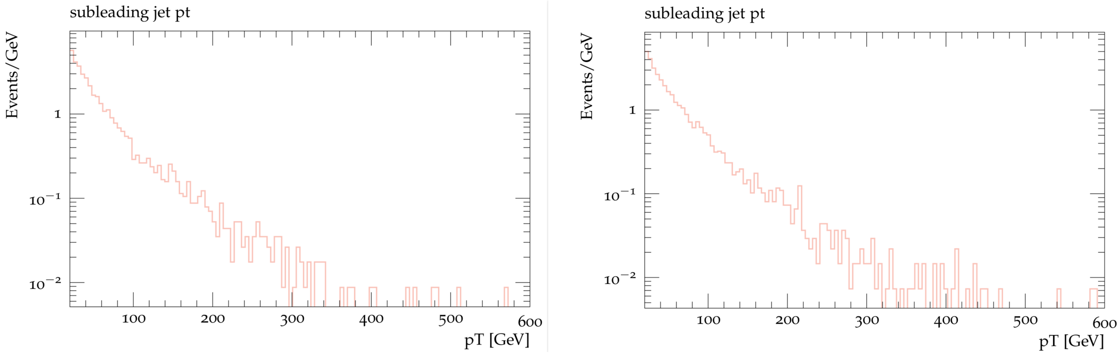

Figure 6.6: Sub-leading jet distribution for 1 and 2 jets processes with xqcut = 10 (left panel) and xqcut = 12 (right panel).

we can see that xqcut = 12 GeV leads to a smoother distribution for $p_{T,sub} < 150$ GeV with no gap around $p_{T,sub} \sim 100$ GeV. This confirms the result shown in Figure 6.5 right panel that xqcut = 12 GeV has the MET shape closer to the ATLAS result.

As a conclusion, the NLO ATLAS simulation on the model as in Table 6.1 can't be fully reproduced due to the limiting computing resources I can access and the lack of detector simulation. Although the merging scheme from the ATLAS side is unknown as well, our single process plus showering result has a reasonable agreement on the fraction of events after the selection cut and bin distribution for majority of the EM regions.

Chapter 7

Conclusions

This thesis is part of my contribution to the decadal 2021 “Snowmass” activities of the American Physical Society. It has presented ways to improve the comparisons of DM experimental sensitivities, where the exclusion limit on the parameter space of DM models or observation related quantities can be regarded as sensitivity of the corresponding experiment. The region where collider exclusion doesn’t rule out all the possibilities in the plane of DM annihilation cross section and DM mass for a pseudo-scalar DM simplified model is identified. A reproduced Fermi limit with respect to each channel’s branching ratio defined by this model is found to have non-significant deviation compared with the Fermi published $b\bar{b}$ result. An outlook on future low g_q DM summary plots is given where different approaches are illustrated including direct translation of limits on signal strength and interpolating upper g_q limits. During this process, a mono-jet Monte Carlo simulation and analysis framework is necessary to validate the signal distribution, as the current mono-jet grid can’t handle the translation for $g_q < 0.05$. The corresponding code is validated and released as a github repository: `https://github.com/Boyu622/MCsetup_monojet.git`

References

[1] G. Bertone et al., Particle dark matter: evidence, candidates and constraints. Physics Reports, 405(5–6):279 – 390, 2005.

[2] G. Jungman et al., Supersymmetric dark matter. Physics Reports, 267(5):195 – 373, 1996.

[3] M. D. Schwartz, Quantum Field Theory and the Standard Model. Cambridge University Press, 2014. ISBN 1107034736, 9781107034730.

[4] A. Boveia and C. Doglioni, Dark Matter Searches at Colliders. Annual Review of Nuclear and Particle Science 68 (2018), no. 1 429–459, [arXiv:1810.12238].

[5] D. Akimov et al., Sensitivity of the COHERENT experiment to accelerator-produced dark matter. Phys. Rev. D 102, 052007 (2020).

[6] T. M. Undagoitia and L. Rauch, Dark matter direct-detection experiments. J. Phys., G43(1):013001, 2016.

[7] The Fermi-LAT Collaboration. The large area telescope on the fermi gamma-ray space telescope mission. Astrophys. J. 697(2009) no 2, 1071.

[8] Ackermann M, et al., Measurement of separate cosmic-ray electron and positron spectra with the Fermi large area telescope. Phys. Rev. Lett., 108:011103, 2012.

[9] The Fermi-LAT Collaboration. Searching for dark matter annihilation from milky way dwarf spheroidal galaxies with six years of fermi large area telescope data. Phys. Rev. Lett., 115:231301, 2015.

[10] The Fermi-LAT, DES Collaborations. Searching for Dark Matter Annihilation in Recently Discovered Milky Way Satellites with Fermi-LAT. Astrophys. J. 834 (2017) no 2, 110.

[11] M. Cirelli et al., PPPC 4 DM ID: a poor particle physicist cookbook for dark matter indirect detection. Journal of Cosmology and Astroparticle Physics 03(2011)051.

[12] K. G. Begeman et al., Extended rotation curves of spiral galaxies-dark haloes and modified dynamics. Monthly Notices of the Royal Astronomical Society, 249:523–537, 1991.

[13] A. Charbonnier et al., Dark matter profiles and annihilation in dwarf spheroidal galaxies: prospectives for present and future γ-ray observatories – I. The classical dwarf spheroidal galaxies. Monthly Notices of the Royal Astronomical Society, Volume 418, Issue 3, December 2011.

[14] J. F. Navarro et al., A Universal Density Profile from Hierarchical Clustering. Astrophys. J. 490, 493 (1997).

[15] N. W. Evans et al., Simple J-factors and D-factors for indirect dark matter detection. Phys. Rev. D 93, 103512 (2016).

[16] J. T. Peebles, P. J. E.; Yu. Primeval adiabatic perturbation in an expanding universe. Astrophysical Journal, 162:815, 1970.

[17] W. Hu and S. Dodelson. Cosmic microwave background anisotropies. Annual Review of Astronomy and Astrophysics, 40(1):171–216, 2002.

[18] Planck Collaboration. Planck 2015 results. Astronomy and Astrophysics, 594:A11, 2016.

[19] A. Boveia et al., Recommendations on presenting LHC searches for missing transverse energy signals using simplified s-channel models of dark matter. Physics of the Dark Universe, 27 (2020) 100365.

[20] A. Albert et al., Recommendations of the LHC Dark Matter Working Group: Comparing LHC searches for heavy mediators of dark matter production in visible and invisible decay channels and calculations of the thermal relic density. Physics of the Dark Universe, 26 (2019) 100377.

[21] D. Abercrombie et al., Dark Matter benchmark models for early LHC Run-2 Searches: Report of the ATLAS/CMS Dark Matter Forum, Physics of the Dark Universe 27 (2020) 100371.

[22] A. Bishop, Using Deep Neural Networks to Classify and Investigate ATLAS Data. `https://www.nevis.columbia.edu/reu/2018/Talk_Abigail_Bishop.pdf`

[23] The ATLAS Collaboration, Search for dark matter and other new phenomena in events with an energetic jet and large missing transverse momentum using the ATLAS detector, Journal of High Energy Physics, 01 (2018) 126.

[24] The ATLAS Collaboration, Search for new phenomena in events with an energetic jet and missing transverse momentum in pp collisions at $\sqrt{s} = 13$ TeV with the ATLAS detector, arXiv:2102.10874.

[25] M. Cacciari, G. P. Salam and G. Soyez, The anti-kt jet clustering algorithm, Journal of High Energy Physics, 04 (2008) 063.

[26] E. Tolley, Search for Evidence of Dark Matter Production in Monojet Events With the ATLAS Detector. http://nrs.harvard.edu/urn-3:HUL.InstRepos:37944978

[27] The ATLAS Collaboration, Search for light dijet resonances with the ATLAS detector using a Trigger-Level Analysis in LHC pp collisions at $\sqrt{s} = 13$ TeV. Phys. Rev. Lett. 121, 081801 (2018).

[28] The ATLAS Collaboration, Search for new phenomena in dijet events using 37 fb^{-1} of pp collision data collected at $\sqrt{s} = 13$ TeV with the ATLAS detector. Phys. Rev. D 96, 052004 (2017).

[29] LUX Collaboration, D. S. Akerib et al., Improved WIMP scattering limits from the LUX experiment. Phys. Rev. Lett. 116, 161301 (2016).

[30] XENON Collaboration, E. Aprile et al., Physics reach of the XENON1T dark matter experiment. Journal of Cosmology and Astroparticle Physics 04(2016)027.

[31] SuperCDMS Collaboration, R. Agnese et al., WIMP-Search Results from the Second CDMSlite Run. Phys. Rev. Lett. 116, 071301 (2016).

[32] CRESST Collaboration, G. Angloher et al., Results on light dark matter particles with a low-threshold CRESST-II detector. Eur. Phys. J. C76 (2016) 25.

[33] CMS Collaboration, Report on the Physics at the HL-LHC and Perspectives for the HE-LHC, arXiv:1902.10229.

[34] P. Harris et al., Closing up on Dark Sectors at Colliders: from 14 to 100 TeV, PRD 93 (2016) 054030.

[35] R. Ellis, et al., Physics Briefing Book: Input for the European Strategy for Particle Physics Update 2020, arXiv:1910.11775.

[36] H.E.S.S. Collaboration, Search for dark matter annihilations towards the inner Galactic halo from 10 years of observations with H.E.S.S, PRL 117 (2016) 111301.

[37] J. Carr et al., Prospects for Indirect Dark Matter Searches with the Cherenkov Telescope Array (CTA), arXiv:1508.06128.

[38] A. Drlica-Wagner et al., Probing the Fundamental Nature of Dark Matter with the Large Synoptic Survey Telescope, arXiv:1902.01055.

[39] L. M. Carpenter et al., Indirect Detection Constraints on s and t Channel Simplified Models of Dark Matter. Phys. Rev. D 94, 055027 (2016).

[40] F. Ambrogi et al., MadDM v.3.0: a Comprehensive Tool for Dark Matter Studies. Phys. Dark Univ. 24 (2019) 100249.

[41] G. D. Martinez, A Robust Determination of Milky Way Satellite Properties using Hierarchical Mass Modeling. Mon. Not. R. Astron. Soc. 451, 2524(2015).

[42] ATLAS Collaboration, Dark matter summary plots : update July 2020, Tech. Rep. ATL-PHYS-PUB-2020-021, CERN, Geneva, Jul, 2020. http://cds.cern.ch/record/2725266.

[43] A. Albert, et al., Displaying dark matter constraints from colliders with varying simplified model parameters. `https://www.snowmass21.org/docs/files/summaries/EF/SNOWMASS21-EF10_EF9_Andreas_Albert-094.pdf`

[44] PICO Collaboration, Dark matter search results from the complete exposure of the PICO-60 C_3F_8 bubble chamber. Phys. Rev. D 100, 022001 (2019).

[45] M. Angelsmark, Studies of Dark Matter Signals at the LHC. `http://lup.lub.lu.se/student-papers/record/8909051`

[46] J. Alwall et al., The automated computation of tree-level and next-to-leading order differential cross sections, and their matching to parton shower simulations. Journal of High Energy Physics 07(2014)079.

[47] R. D. Ball et al., Parton distributions with LHC data. Nucl. Phys. B 867 (2013) 244.

[48] T. Sjöstrand et al., A Brief Introduction to PYTHIA 8.1. Comput. Phys. Commun. 178 (2008) 852-867.

[49] E. Conte et al., MadAnalysis 5, a user-friendly framework for collider phenomenology. Comput. Phys. Commun. 184 (2013) 222-256.

[50] A. Buckley et al., Rivet user manual. Comput. Phys. Commun. 184 (2013) 2803-2819.

[51] M. Zaro et al., MadGraph5_aMC@NLO tutorial. https://indico.cern.ch/event/555228/sessions/203428/attachments/1315471/1970459/tutorial-CMSandATLAS-2016.pdf

[52] J. Alwall et al., Comparative study of various algorithms for the merging of parton showers and matrix elements in hadronic collisions. Eur. Phys. J. C53 (2008) 473-500.

[53] Mawatari. http://feynrules.irmp.ucl.ac.be/attachment/wiki/DMsimp/DMsimp_s_spin1_v2.0.zip

[54] Rosa Seoane, Z'-explorer: confronting Z' models against LHC data. https://indico.cern.ch/event/982553/contributions/4219481/